

p-side QWs. The experimental results were well reproduced by Monte-Carlo numerical simulations with a finite resonance line-width (data not shown).

To observe the temporal correlation between the modulation input and photon emission, we measured the time delay from the rising edge of the modulation input to the photon detection event at the first current plateau ( $I = ef$ ) and at the second current plateau ( $I = 2ef$ ). The probability of a single electron-hole pair injected to the central QW of the turnstile device being detected as a photon in the detector was  $\sim 1 \times 10^{-4}$  owing to a poor optical coupling efficiency between the two devices in the present set-up. However, the detection quantum efficiency does not affect the time correlation characteristics. Histograms of the measured time delay with 10-MHz modulation frequency are shown in Fig. 3a (for  $I = ef$ ) and Fig. 3c (for  $I = 2ef$ ). The photon emission probabilities have peaks near the rising edge of the modulation input. The rapid increase of the photon emission probability is associated with the hole tunnelling time ( $\tau_h \approx 4$  ns), and the slow decay of the photon emission probability corresponds to the electron-hole recombination lifetime ( $\tau_{ph} \approx 25$  ns: due to both radiative and non-radiative processes). The photon emission probability in Fig. 3a decays to a non-zero value during the on-pulse due to photons generated by background current. The ratio of the counts contained in the peak to those contained in the non-zero background is  $\sim 3:1$ , consistent with the ratio of the turnstile current to the background current in this device. The second and faster decay for  $I = 2ef$  (Fig. 3c) represents the decay of the hole via backward tunnelling and electron-hole recombination. The associated lifetime for this decay is  $(\tau_h^{-1} + \tau_{ph}^{-1})^{-1}$ . The dashed lines show the analytical solutions using these parameters.

The experimental results, as well as the analytical traces, are well reproduced by Monte Carlo numerical simulations, as shown in Fig. 3b ( $I = ef$ ) and Fig. 3d ( $I = 2ef$ ). The fact that the photon emission probability decreases during the duration of the on-pulse is a unique indication that the number of holes injected during an on-pulse is restricted to either one or two due to the Coulomb blockade effect (Fig. 4 of Supplementary Information). Figure 3e shows the experimental result for a larger-area device at a higher temperature of 4 K, where the Coulomb blockade effect is absent. In this case, arbitrary numbers of holes are allowed to tunnel into the central QW during an on-pulse, and so the resulting photon emission probability should increase monotonically with a time constant  $\tau_{ph}$  to the steady-state value. This result is well-reproduced by the simulation (Fig. 3f).

The experimental results reported here provide evidence for the long-sought generation of regulated streams of single photons (and  $n$ -photons) where the time interval between single photons is regulated to beyond the Poisson limit. If the un-regulated background photons were suppressed and the collection efficiency was improved, such a non-classical photon source could provide an efficient source for future quantum information technologies, and could also be a useful tool for fundamental tests of quantum mechanics. □

Received 5 August; accepted 7 December 1998.

- Hanbury Brown, R. & Twiss, R. Q. Correlation between photons in two coherent beams of light. *Nature* **177**, 27–29 (1956).
- Reznikov, M., Heiblum, M., Shtrikman, H. & Mahalu, D. Temporal correlation of electrons: suppression of shot noise in a ballistic quantum point contact. *Phys. Rev. Lett.* **75**, 3340–3343 (1995).
- Kumar, A., Saminadayar, L., Glattli, D. C., Jin, Y. & Etienne, B. Experimental test of the quantum shot noise reduction theory. *Phys. Rev. Lett.* **76**, 2778–2781 (1996).
- Liu, R. C., Odom, B., Yamamoto, Y. & Tarucha, S. Quantum interference in electron collision. *Nature* **391**, 263–265 (1998).
- Walls, D. F. & Milburn, G. J. *Quantum Optics* (Springer, Berlin, 1994).
- Imamoglu, A. & Yamamoto, Y. Turnstile device for heralded single photons: Coulomb blockade of electron and hole tunneling in quantum confined  $p$ - $i$ - $n$  heterojunctions. *Phys. Rev. Lett.* **72**, 210–213 (1994).
- Imamoglu, A., Schmidt, H., Woods, G. & Deutsch, M. Strongly interacting photons in a nonlinear cavity. *Phys. Rev. Lett.* **79**, 1467–1470 (1997).
- Yamamoto, Y. A photon in solitary confinement. *Nature* **390**, 17–18 (1997).
- von Klitzing, K., Dorda, G. & Pepper, M. New method for high-accuracy determination of the fine-structure constant based on quantized Hall resistance. *Phys. Rev. Lett.* **45**, 494–497 (1980).

- Yamamoto, Y. in *Quantum Optics of Confined Systems* (eds Ducloy, M. & Bloch, D.) 201–281 (Kluwer, Dordrecht, 1996).
- Beenakker, C. W. J. & Büttiker, M. Suppression of shot noise in metallic diffusive conductors. *Phys. Rev. B* **46**, 1889–1892 (1992).
- Liu, R. C. & Yamamoto, Y. Suppression of quantum partition noise in mesoscopic electron branching circuits. *Phys. Rev. B* **49**, 10520–10532 (1994).
- Imamoglu, A. & Yamamoto, Y. Noise suppression in semiconductor  $p$ - $i$ - $n$  junctions: Transition from macroscopic squeezing to mesoscopic Coulomb blockade of electron emission process. *Phys. Rev. Lett.* **70**, 3327–3330 (1993).
- Kim, J., Kan, H. & Yamamoto, Y. Macroscopic Coulomb-blockade effect in a constant-current-driven light-emitting diode. *Phys. Rev. B* **52**, 2008–2012 (1995).
- Kim, J. & Yamamoto, Y. Theory of noise in  $p$ - $n$  junction light emitters. *Phys. Rev. B* **55**, 9949–9959 (1997).
- Delsing, P., Likharev, K. K., Kuzmin, L. S. & Claeson, T. Time-correlated single-electron tunneling in one-dimensional arrays of ultrasmall tunnel junctions. *Phys. Rev. Lett.* **63**, 1861–1864 (1989).
- Geerligs, L. J. et al. Frequency-locked turnstile device for single electrons. *Phys. Rev. Lett.* **64**, 2691–2694 (1990).
- Kouwenhoven, L. P. et al. Quantized current in a quantum-dot turnstile using oscillating tunnel barriers. *Phys. Rev. Lett.* **67**, 1626–1629 (1991).
- Hobson, W. S. et al. Silicon nitride encapsulation of sulfide passivated GaAs/AlGaAs microdisk lasers. *J. Vac. Sci. Technol. A* **13**, 642–645 (1995).
- Kim, J., Yamamoto, Y. & Hogue, H. H. Noise-free avalanche multiplication in Si solid state photomultipliers. *Appl. Phys. Lett.* **70**, 2852–2854 (1997).

Supplementary information is available on Nature's World-Wide Web site (<http://www.nature.com>) or as paper copy from the London editorial office of Nature.

Acknowledgements. We thank H. H. Hogue for providing us with SSPM detectors. This work was partially supported by JSEP.

Correspondence and requests for materials should be addressed to Y.Y. ([yamamoto@loki.stanford.edu](mailto:yamamoto@loki.stanford.edu)).

## Modulated phases and proton centring in ice observed by X-ray diffraction up to 170 GPa

Paul Loubeyre<sup>\*†</sup>, René LeToullec<sup>†</sup>, Elodie Wolanin<sup>†</sup>, Michel Hanfland<sup>‡</sup> & Daniel Hausermann<sup>‡</sup>

<sup>\*</sup>Laboratoire Etats Extrêmes Statiques, SPMC/DPTA, CEA 91680 Bruyères-le-Châtel, France

<sup>†</sup>CNRS and Université Paris 6, PMC boîte 77, 4 place Jussieu 75252 Paris, France

<sup>‡</sup>ESRF, BP 220, 38043 Grenoble, France

Because of its open hydrogen-bonded structure, ice shows many structural changes between different crystalline forms under high pressure. Crystallographic studies of these transitions have been pursued largely by neutron scattering, which allows the positions of the hydrogen atoms to be identified<sup>1,2</sup>. Such studies have previously been extended to pressures of up to 20 GPa, which is however insufficient to permit the investigation of ice X, a 'symmetric ice' in which the protons are thought to reside midway between the oxygen atoms<sup>3–5</sup>. So far, information about ice X has therefore come from indirect methods such as infrared<sup>6,7</sup> or Brillouin<sup>8</sup> spectroscopy. Here we show that single-crystal X-ray diffraction is able to reveal the signature of hydrogen-bond symmetrization. The 111 reflection can be assigned to the hydrogen atoms alone, and we can measure it up to 170 GPa in a diamond anvil cell. This diffraction line (normalized against the intensity of the 222 line, which is due mostly to oxygen atoms) indicates that the proton centring in ice X occurs from about 60 to 150 GPa; at this latter pressure the intensity increases sharply, signalling a further structural change. At lower pressures, we see ice VII ordering in a sequence of spatially modulated phases between 2.2 and 25 GPa, which suggests an analogy with the incommensurate phases of the frustrated Ising model<sup>9</sup>.

We use the single-crystal X-ray diffraction technique with the high brilliance of the European Synchrotron Radiation Facility to measure the structural properties of ice VII in a diamond anvil cell at very high pressure, as described previously for solid hydrogen<sup>10</sup>. Ice VII is the stable form of ice at ambient temperature above 2.2 GPa, but its detailed nature remains unknown, with possible multisite disorder of both the oxygen and hydrogen atoms<sup>2</sup>. The single crystal was grown by looking optically at the solid–fluid

equilibrium on the melting curve of ice VII, with no preferential orientation for the growth. Embedding the single crystal in a quasihydrostatic cushion—here we used gold in a ring around the crystal rather than He because of the formation of clathrates—is necessary to significantly reduce its fragmentation up to the 100 GPa range. Good hydrostatic conditions could be achieved up to 20 GPa, but non-hydrostatic compression was observed at higher pressures. Three experiments were performed to determine the equation of state (EOS) of ice at very high pressure. At least six classes of reflections were observed up to 170 GPa and related by the cubic orientation matrix as  $\langle 110 \rangle$ ,  $\langle 220 \rangle$ ,  $\langle 111 \rangle$ ,  $\langle 222 \rangle$ ,  $\langle 200 \rangle$  and  $\langle 121 \rangle$ . The diffraction data are consistent with the body-centred-cubic oxygen sublattice persisting up to 170 GPa. In Fig. 1, the single-crystal measurements of the lattice parameter of the cubic unit cell are compared with those performed on a powdered sample up to a maximum pressure of 128 GPa (refs 11, 12). The good agreement between these different sets of data gives confidence that a correct determination of the EOS of ice can be reached, even though

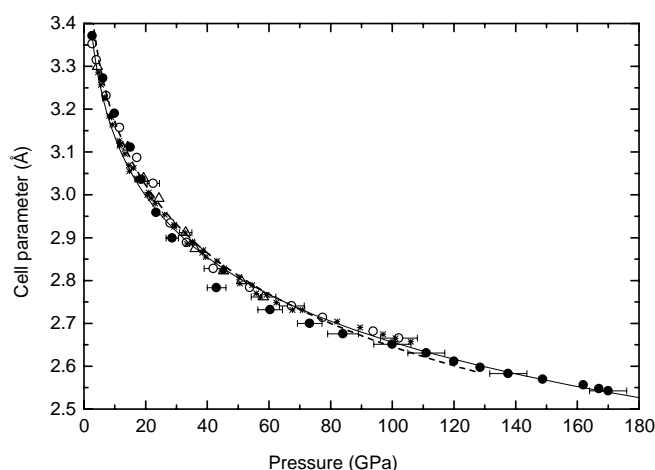


**Figure 1** The pressure-cell parameter relation in ice at 300 K. Filled circles, open circles and open triangles indicate results of three single-crystal experiments; asterisks show measurements on powdered ice<sup>12</sup>. The dashed line is a good fit to data from ref. 11 up to 128 GPa. A Vinet form<sup>17</sup>—promoted as a universal equation of state for solids under strong compression—is satisfactorily applied here to represent the data within the dispersion of the various determinations, shown as the solid line ( $V = a^3/2$ ). It is given by:

$$P = 3K_0 \left( \frac{V}{V_0} \right)^{-2/3} \left( 1 - \left( \frac{V}{V_0} \right)^{1/3} \right) \exp \left( \frac{3}{2} (K'_0 - 1) \left( 1 - \left( \frac{V}{V_0} \right)^{1/3} \right) \right)$$

with  $V_0 = 14.52 \text{ cm}^3 \text{ mol}^{-1}$  ( $a_0 = 3.64 \text{ Å}$ ),  $K_0 = 4.26 \text{ GPa}$ ,  $K'_0 = 7.75$ . The pressure was determined by both the non-hydrostatic ruby<sup>18</sup> and the  $\text{SrB}_2\text{O}_7\text{:Sm}^{2+}$  (ref. 19) luminescence pressure scales, and also by the Au molar volume (estimated from the 111 and 002 diffraction peaks) related to the pressure through the Au equation of state<sup>20</sup>. The X-ray beam was collimated by microslits down to  $15 \times 15 \text{ μm}$ . correction for the pressure gradient was estimated from the variation of the  $d$ -spacings of the strong 110 peak within the  $\text{H}_2\text{O}$  single crystal. The error bar in the pressure measurement increases from around  $\pm 2 \text{ GPa}$  at 50 GPa to  $\pm 6 \text{ GPa}$  at 170 GPa. The effect of the non-hydrostatic stress leads to a 3% dispersion for the lattice parameter in the 100 GPa range. A stress analysis, based on a simple elastic-type calculus and on the use of the elastic coefficients of ice VII measured up to 7 GPa (ref. 21) and linearly extrapolated with pressure above this, was performed to obtain the correct value of the cell parameter. The value of the uniaxial stress component and of the corresponding hydrostatic lattice parameter were fitted by least squares. A solution could always be found that reproduces the observed  $d$ -spacings very well. The difference between the corrected volume and the volume estimated from the mean value of the lattice parameter calculated over the various reflections was  $\sim 1\%$  in the 100 GPa range. Hence, half of it (0.5%) should maximize the size of the error bar for the volume determination above 30 GPa.

corrections for the pressure gradient and for the effect of the uniaxial stress have to be made. Extending the measurements to 170 GPa allows the EOS to be determined more accurately.

The single-crystal X-ray diffraction pattern associated with the 222 reflection is presented in Fig. 2, top inset; two other reflections are also clearly seen. The 111 reflection has been observed in neutron diffraction studies<sup>1</sup>. (Its intensity change will be analysed below.) In contrast, the superlattice reflection at nearly  $\frac{1}{2}\frac{1}{2}\frac{1}{2}$  was a surprise. Its  $d$ -spacing is slightly different from the value expected from a doubling of the unit cell, indicating a periodic modulation of the structure along the  $[111]$  direction. The evolution with pressure of this peak (which we denote as  $S_{\frac{1}{2}\frac{1}{2}\frac{1}{2}}$ ) was studied for three large single crystals (using 500- $\text{μm}$  anvil-tip diameter) under hydrostatic compression. The following observations will support the interpretation proposed below. The  $S_{\frac{1}{2}\frac{1}{2}\frac{1}{2}}$  peak could be measured in all the four  $[111]$  directions accessible within the X-ray aperture of the diamond anvil cell, with identical  $d$ -spacings (within error limits) and very similar intensity. Neither the  $\frac{1}{4}\frac{1}{4}\frac{1}{4}$  reflection nor a similar modulation in the  $[110]$ ,  $[200]$  or  $[121]$  directions could be detected. No distortion from the cubic structure was observed. The periodicity of the modulation,  $d_{\frac{1}{2}\frac{1}{2}\frac{1}{2}}/4d_{222}$ , is plotted versus pressure in the main part of Fig. 2. The change with pressure is continuous and very reproducible between the three samples up to 8 GPa, independent of the orientation of the crystal with respect to the load axis on the diamond anvils or of the thickness of the gold ring in the sample chamber. Also, the  $S_{\frac{1}{2}\frac{1}{2}\frac{1}{2}}$  peak was observed in each run at the pressure when the single crystal started to grow from the melt. These two last observations rule out the possibility that this new peak might be produced by uniaxial stress. We believe that the modulated phases are intrinsic properties of ice VII that tend to disappear in a strained crystal or in powdered ice. Between 10 and 20 GPa, the modulation seems to show lock-in plateaux, as predicted by theories of modulated systems<sup>9,13</sup>; we note that this corresponds to the pressure range where the  $S_{\frac{1}{2}\frac{1}{2}\frac{1}{2}}$  peak has maximum intensity (Fig. 2 inset).

We consider that there is an analogy between the present observations and the phase diagram of the three-dimensional Ising model with competing interactions<sup>9</sup>. First, calculations showed that a large fraction of the phase diagram of the Ising model is formed by the ‘++--++’ phase, consisting of two ‘up’ layers followed by two ‘down’ layers and so on. At low temperature, ice VII transforms into a closely related structure<sup>1</sup>, ice VIII, which is

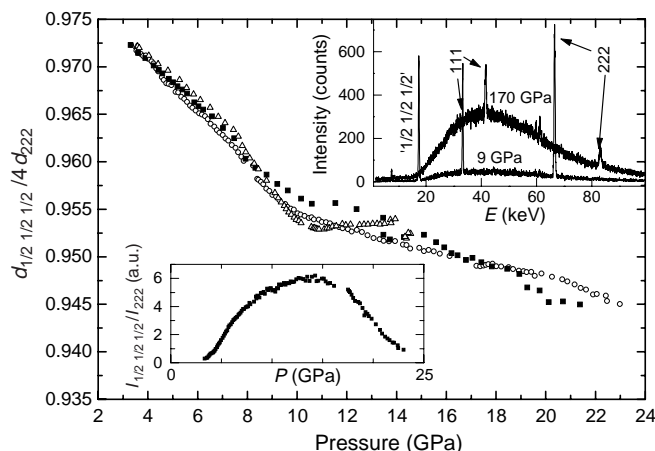


**Figure 2** Periodicity of the modulation  $S_{\frac{1}{2}\frac{1}{2}\frac{1}{2}}$  versus pressure in ice VII at 300 K. Main figure, variation with pressure of the ratio of the  $d$ -spacing of the peak  $S_{\frac{1}{2}\frac{1}{2}\frac{1}{2}}$  to its ideal value. Measurements on three different samples are indicated by three different symbols. Top inset, single-crystal energy-dispersive spectra for the 222 reflection at 9 GPa and 170 GPa. The 111 and  $S_{\frac{1}{2}\frac{1}{2}\frac{1}{2}}$  peaks are also clearly identified. Bottom inset, evolution with pressure of the intensity of the  $S_{\frac{1}{2}\frac{1}{2}\frac{1}{2}}$  reflection relative to that of the 222 reflection (not corrected for the wiggler energy spectrum).

a dipole-ordered antiferroelectric solid. The dipole ordering is accompanied by a slight tetragonal distortion of the cubic unit cell. The 202 peak of ice VIII corresponds to the 111 peak of ice VII, and the allowed 101 peak of ice VIII (weakly measured on powder with X-rays and with a  $d$ -spacing exactly twice that of the 202 peak) corresponds to the forbidden  $\frac{111}{222}$  peak of ice VII. Hence, neglecting the tetragonal distortion, the arrangement of the dipoles in ice VIII can be seen as a ‘++--++’ order, consisting of two quasi-(111) layers where the dipoles point positively along the [001] direction, followed by two quasi-( $\bar{1}\bar{1}\bar{1}$ ) layers where the dipoles point negatively along the [001] direction. Second, as the ratio of the competing next-nearest-neighbour interaction to the nearest-neighbour interaction is changed, the Ising model displays a sequence of spatially modulated phases; the periodicity of the modulation changes quasi-continuously with the ratio of the interactions. So in ice VII we could be observing an interesting stability field of modulated phases around the ‘++--++’ ice VIII phase, due to the magnitudes of the competing dipolar interactions being changed by pressure. Unravelling the detailed arrangement of hydrogen atoms is beyond the present experimental study, but the [111] directions now appear as the axes around which to construct models of disorder in ice VII.

As seen in Fig. 2, top inset, the 111 peak can be clearly followed up to 170 GPa. The calculation of the structure factor shows that its intensity can be considered as entirely due to the hydrogens, because the contribution of the oxygen atoms (even when taking into account possible oxygen disorder) is at most 1% of the total intensity of the peak. The measured change in the ratio of the intensity of the 111 peak to that of the 222 peak,  $I_{111}/I_{222}$ , should be quite accurate in the present single-crystal technique. The evolution of  $I_{111}/I_{222}$  with pressure (measured on two [111] directions with good agreement) is shown in Fig. 3. In an isolated-atom approximation of the structure factor,  $I_{111}/I_{222}$  should continuously increase by a factor of about 3 as H moves from its position in ice VII towards

the centre of the two oxygens. Trying to model more realistically the O–H covalent bonding and its change with pressure, by placing charges half-way between O and H, has only a small effect—at maximum, a 20% change in the factor 3 of the increase (when  $\frac{1}{2}$  an electron is placed at the mid-point of the O–H bond). Taking into account the quantum smearing of the proton due to tunnelling<sup>5</sup> lessens this ratio by 10% at most. Finally, a plausible way to reach an increase of around 5 for  $I_{111}/I_{222}$  is to model the oxygen atoms as disordered over displaced sites. We can therefore confidently state that the evolution of  $I_{111}/I_{222}$  from 1 to a plateau at around 3 is the signature of the transition to symmetric ice, ice X. We note that the structure factor calculation, taking into account the experimental inputs of the EOS and of the small change of the O–H bond-length, ( $d_{\text{O-H}}$ ) with pressure<sup>14</sup> measured up to 20 GPa, gives a linear increase to a 50% variation of  $I_{111}/I_{222}$  at 20 GPa. We can now interpret the data in Fig. 3. (1) The linear fit through the experimental points up to at least 20 GPa reflects the very small variation of  $d_{\text{O-H}}$  in this pressure range<sup>2,14</sup>. (2) The plateau of  $I_{111}/I_{222}$  at a value of about 3 reveals the stability domain of ice X over the pressure range about 60 GPa. This is in very good agreement with the infrared absorption studies<sup>6,7</sup> that provided evidence of changes in the infrared spectra at  $\sim 67$  GPa, subsequently identified by an *ab initio* calculation as the fingerprints of the stability of ice X (ref. 15). However, the transformation from ice VII to ice X can be more or less sluggish. In our good single-crystal experiment (filled circles), the transition was more sudden and correspondingly the lattice parameter in the pressure range 30–70 GPa falls below the average EOS in Fig. 1. In this case, the transition to ice X occurs as low as about 40 GPa, in agreement with a previous claim from Brillouin spectroscopy<sup>8</sup>. In another case, when the crystal is broken up, the transformation could take place through the formation of a dipolar glass, as proposed previously<sup>12</sup>. (3) The rapid rise of  $I_{111}/I_{222}$  at pressures greater than 150 GPa could indicate that a displacive phase transition is taking place, such as the recently predicted body-centred-cubic/hexagonal-close packed transformation path for the oxygens with the hydrogens rigidly following this displacement in between two oxygens<sup>16</sup>. An onset of oxygen site disordering, associated with a large anharmonicity, could also explain the resonance and intensity change observed in the infrared spectra at around 150 GPa (ref. 7). Unfortunately, the change on the  $d$ -spacings was too small to be detected at the beginning of this transformation.

The centring process is visualized in Fig. 3 inset by plotting  $d_{\text{O-H}}$  versus the nearest-neighbour O–O distance,  $d_{\text{O-O}}$ . The stability of ice X at around 65 GPa implies that  $d_{\text{O-H}}$  becomes equal to  $d_{\text{O-O}}/2$  at that pressure. This point complements the neutron data up to 20 GPa<sup>2,14</sup>. The results from our experiment are compared with a very rough approximation of  $d_{\text{O-H}}$  versus  $d_{\text{O-O}}$ , calculated from the assumption that the small linear increase of  $d_{\text{O-D}}$  with pressure measured<sup>14</sup> up to 20 GPa can be extrapolated to very high pressure; the predictions of the recent quantum simulation<sup>5</sup> are also shown in this inset. It is clear that the very small variation of  $d_{\text{O-H}}$  with pressure measured to 20 GPa is strongly accelerated in approaching ice X, in agreement with an O–H stretching mode softening at the transition<sup>6</sup>. We note that the structural transformation to ice X seems to be accurately described by path-integral *ab initio* simulations<sup>5</sup>, indicating that a detailed understanding of quantum effects in proton transfer systems is within the capabilities of numerical methods. □

Received 27 January; accepted 12 October 1998.

- Kuhs, W. F., Finney, J. L., Vettier, C. & Bliss, D. V. Structure and hydrogen ordering in ices VI, VII and VIII by neutron powder diffraction. *J. Chem. Phys.* **81**, 3612–3623 (1984).
- Nelmes, R. J., Loveday, J. S., Marshall, W. G., Hamel, G., Besson, J. N. & Klotz, S. Multisite disordered structure of ice VII to 20 GPa. *Phys. Rev. Lett.* **81**, 2719–2722 (1998).
- Holzappel, W. B. On the symmetry of the hydrogen bonds in ice VII. *J. Chem. Phys.* **56**, 712–715 (1972).
- Schweizer, K. S. & Stillinger, F. H. High pressure phase transitions and hydrogen-bond symmetry in ice polymorphs. *J. Chem. Phys.* **80**, 1230–1240 (1984).

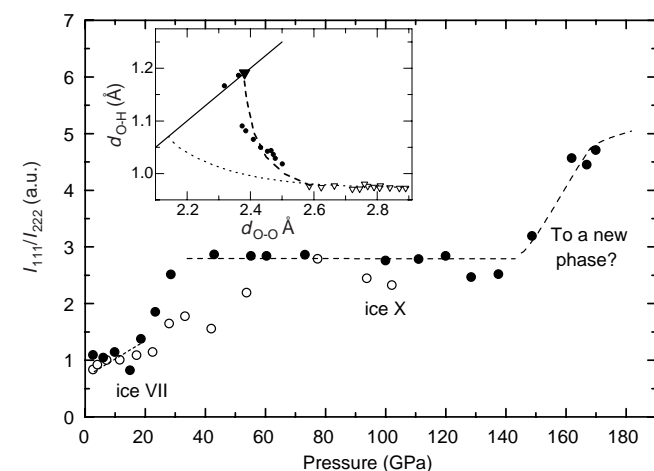


**Figure 3** Proton ordering with pressure in ice at 300K from the intensity change of the 111 reflection. Main figure, evolution with pressure of the ratio of the intensity of the 111 reflection to the intensity of the 222 reflection (in arbitrary unit), reflecting changes in proton ordering. The linear dashed line up to 20 GPa represents the atomic structure-factor calculation with experimental  $d_{\text{O-H}}$  (refs 2, 14). The plateau at  $\sim 3$  is the signature of ice X. Inset, evolution of  $d_{\text{O-H}}$  versus  $d_{\text{O-O}}$ . The triangles are the neutron data<sup>2,14</sup> (because tunnelling is not expected to play a role in this pressure range, the O–H bond-length should not be significantly different). The filled triangle is the data deduced from the volume determination at the centring pressure, 65 GPa. The filled circles correspond to the quantum simulations<sup>5</sup>. The dotted line represents the simple empirical model based on the extrapolation of the constant linear variation of  $d_{\text{O-H}}$ . The dashed line is a reasonable interpolation between experimental data. The symmetrization line,  $d_{\text{O-H}} = d_{\text{O-O}}/2$ , is indicated (solid line).



5. Benoit, M., Marx, D. & Parrinello, M. Tunnelling and zero-point motion in high-pressure ice. *Nature* **392**, 258–261 (1998).
6. Aoki, K., Yamawaki, H., Sakashita, M. & Fujihisa, H. Infrared absorption study of the hydrogen-bond symmetrization in ice to 100 GPa. *Phys. Rev. B* **54**, 15673–15677 (1996).
7. Goncharov, A. F., Struzhkin, V. V., Somayazulu, M. S., Hemley, R. J. & Mao, H. K. Compression of ice to 210 GPa: Infrared evidence for a symmetric hydrogen-bonded phase. *Science* **273**, 218–220 (1996).
8. Polian, A. & Grimsditch, M. New high pressure phase of H<sub>2</sub>O: Ice X. *Phys. Rev. Lett.* **52**, 1312–1314 (1984).
9. Bak, P. & von Boehm, J. Ising model with solitons, phasons and 'the devil's staircase'. *Phys. Rev. B* **21**, 5297–5308 (1980).
10. Loubeyre, P. *et al.* X-ray diffraction and equation of state of hydrogen at megabar pressures. *Nature* **383**, 702–704 (1996).
11. Hemley, R. J. *et al.* Static compression of H<sub>2</sub>O-ice to 128 GPa. *Nature* **330**, 737–740 (1987).
12. Wolanin, E. *et al.* Equation of state of ice VII up to 106 GPa. *Phys. Rev. B* **56**, 5781–5785 (1997).
13. Aubry, S. Devil's staircase and order without periodicity in classical condensed matter. *J. Phys. (Paris)* **44**, 147–162 (1983).
14. Nemes, R. J. *et al.* Neutron diffraction study of the structure of deuterated ice VIII to 10 GPa. *Phys. Rev. Lett.* **71**, 1192–1195 (1993).
15. Bernasconi, M., Silvestrelli, P. L. & Parrinello, M. Ab-initio infrared absorption study of the hydrogen-bond symmetrization in ice. *Phys. Rev. Lett.* **81**, 1235–1238 (1998).
16. Benoit, M., Bernasconi, M., Focher, P. & Parrinello, M. New high pressure phase of ice. *Phys. Rev. Lett.* **76**, 2934–2936 (1996).
17. Vinet, P., Ferrante, J., Smith, J. R. & Rose, J. H. A universal equation of state for solids. *J. Phys. C* **19**, L467–L473 (1986).
18. Mao, H. K., Bell, P. M., Shaner, J. & Steinberg, D. Specific volume measurements of Cu, Mo, Pd and Ag and calibration of the ruby R1 fluorescence pressure gauge from 0.06 to 1 Mbar. *J. Appl. Phys.* **49**, 3276–3283 (1978).
19. Datchi, F., LeToullec, R. & Loubeyre, P. Improved calibration of the SrB<sub>4</sub>O<sub>7</sub>:Sm<sup>2+</sup> optical pressure gauge: Advantages at very high pressures and high temperatures. *J. Appl. Phys.* **81**, 3333–3339 (1997).
20. Anderson, O. L., Isaak, O. & Yamamoto, S. Anharmonicity and the equation of state of gold. *J. Appl. Phys.* **65**, 1534–1543 (1989).
21. Shimizu, H., Nabetani, T., Nishiba, T. & Sasaki, S. High pressure elastic properties of the VI and VII phase of ice in dense H<sub>2</sub>O and D<sub>2</sub>O. *Phys. Rev. B* **53**, 6107–6110 (1996).

**Acknowledgements.** We thank J. Loveday for the computation of the effect of oxygen disorder and proton tunnelling on the structure factor, F. Datchi for help in the experiments and the ESRF staff for technical support. We also thank Y. Petroff for continuous interest in this work, and Ph. Pruzan and J. M. Besson for discussions. We acknowledge a referee for suggesting the interpretation of the rise in  $I_{111}/I_{222}$  at 150 GPa.

Correspondence and requests for materials should be addressed to P.L. (paul.loubeyre@bruyeres cea.fr).

## Circularly polarized light generated by photoexcitation of luminophores in glassy liquid-crystal films

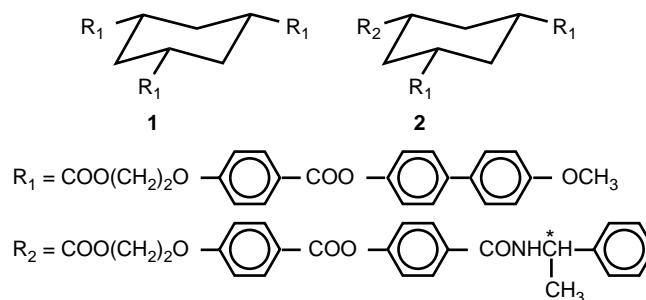
S. H. Chen<sup>†‡§</sup>, D. Katsis<sup>†</sup>, A. W. Schmid<sup>‡</sup>, J. C. Mastrangelo<sup>§</sup>, T. Tsutsui<sup>||</sup> & T. N. Blanton<sup>¶</sup>

<sup>\*</sup> Materials Science Program, <sup>†</sup> Department of Chemical Engineering, <sup>‡</sup> Laboratory for Laser Energetics, <sup>§</sup> NSF Center for Photoinduced Charge Transfer, Center for Optoelectronics and Imaging, University of Rochester, 240 East River Road, Rochester, New York 14623-1212, USA  
<sup>||</sup> Department of Applied Science for Electronics and Materials, Kyushu University, Kasuga, Fukuoka 816-8580, Japan  
<sup>¶</sup> Analytical Technology Division, Kodak Research Laboratories B82A, Eastman Kodak Company, Rochester, New York 14650-2106, USA

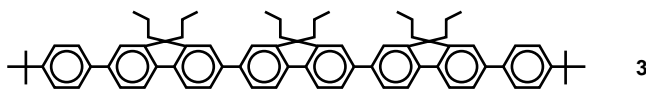
Optical information processing, display and storage can be accomplished with linearly or circularly polarized light. In passive (non-emitting) devices, linear polarization can be produced by anisotropic absorption of light<sup>1</sup>, whereas circular polarization has been attained by selective reflection of unpolarized light propagating through a chiral-nematic liquid-crystal film<sup>2</sup>. Active (light-emitting) devices capable of polarized emission are also needed. In principle, optical and electronic excitation of materials containing uniaxially and helically arranged luminophores should produce linearly and circularly polarized emission, respectively. In practice, the former is easier to achieve and is therefore more technologically advanced<sup>3–8</sup>. Here we report the generation of strongly circularly polarized photoluminescence from films of glass-forming chiral-nematic liquid crystals<sup>9</sup> in which are embedded light-emitting dopants. This host material apparently induced alignment of the luminophores to a degree that produces almost pure circular polarization within the 400–420-nm wave-

length band of the emitted light. We anticipate that composite films of this sort might find applications within photonic technology such as colour-image projection<sup>10</sup> and stereoscopic displays<sup>11</sup>.

As a measure of the degree of circularly polarized photoluminescence (CPPL), the dissymmetry factor,  $g_c$ , is defined as  $2(I_L - I_R)/(I_L + I_R)$ , where  $I_R$  and  $I_L$  denote respectively the right- and left-handed emission intensity. It is evident that  $|g_c|$  equals 2 for pure, single-handed CPPL. Polythiophene with chiral pendants in solution<sup>12</sup> and chiral-nematic fluid films doped with a fluorescent dye<sup>13</sup> have been found to produce a  $g_c$  value of  $5.0 \times 10^{-3}$  and 0.8, respectively. Circularly polarized electroluminescence has also been demonstrated using a thin film of poly(*p*-phenylene vinylene) with chiral pendants, yielding a  $g_c$  value of  $1.7 \times 10^{-3}$  (ref. 14). All these previous studies have been restricted to emission outside the selective reflection band (that is, outside the resonance region). Here we study photoluminescence inside the resonance region. A nematic and a chiral-nematic glass-forming liquid crystal (GLC) depicted respectively as **1** and **2** below, were synthesized as part of our recent work on GLCs as an emerging class of optical materials<sup>9</sup>:



As a light-emitting dopant, Exalite 428 (Exciton, Inc., Dayton, Ohio, USA) with the following structure was used:



Compound **3** has an absorption peak at 360 nm with an extinction coefficient of  $1.30 \times 10^5 \text{ M}^{-1} \text{ cm}^{-1}$ , and an emission peak covering 380 to 500 nm with excitation at 360 nm; these properties were obtained from a  $10^{-5} \text{ M}$  solution of **3** in methylene chloride. A series of chiral-nematic hosts with a wide range of selective reflection wavelength ( $\lambda_R$ ) were prepared by dissolving various ratios of **1** and **2** in methylene chloride. Doping of the chiral-nematic hosts with Exalite 428 at a level of 0.2 wt% was also accomplished by co-dissolution: solid samples were collected by evaporating off the solvent *in vacuo*. The thermotropic properties and the measured values of  $\lambda_R$  of the GLC hosts, (I) to (V), are summarized in Table 1.

**Table 1 Chemical composition and properties of GLC hosts**

GLC host	<b>1</b> (wt%)	<b>2</b> (wt%)	DSC* (°C)	$\lambda_R^\dagger$ (nm)
(I)	0	100	G 77 Ch 147 I	410
(II)	5	95	G 75 Ch 154 I	434
(III)	49	51	G 68 Ch 215 I	890
(IV)	62	38	G 67 Ch 235 I	1210
(V)	100	0	G 64, 95 K <sub>1</sub> 130 K <sub>2</sub> 180 N 279 I†	α

Formulae of compounds **1** and **2** are given in the text.

\* Thermal transition temperatures were determined from DSC second heating scans at  $50^\circ \text{C min}^{-1}$  of samples preheated to  $250^\circ \text{C}$  followed by quenching at  $-60^\circ \text{C min}^{-1}$  to  $-30^\circ \text{C}$ ; the nematic and cholesteric mesophases were identified as threaded textures and oily streaks, respectively, under polarizing optical microscopy. Symbols: G, glassy; K, crystalline; Ch, cholesteric; N, nematic; I, isotropic.

† Selective reflection wavelength,  $\lambda_R$ , was determined for 14-μm-thick film by ultraviolet-visible spectrophotometry.

‡ Recrystallization at  $130^\circ \text{C}$  and crystalline modification at  $180^\circ \text{C}$  were observed in the DSC heating scan of vitrified (V) at  $50^\circ \text{C min}^{-1}$ .